INTRODUCTION

Above Earth's atmosphere are the a pair of Van Allen radiation belts, a complex and dynamic plasma environment that affects our technology-driven society. These effects include: a higher radiation dose for astronauts and cosmonauts, higher chance of spacecraft failure due to single event upsets that can lead to catastrophic latchups, degradation of silicon (changing the silicon doping) from an extended radiation dose that can degrade a transistor to the point where it no longer function as a switch, and the degradation of the ozone layer due to the chemical production of NO_X and HO_X molecules. With these effects in mind, it is no surprise that the radiation belts have been extensively studied since their discovery in the 1960s.

One natural phenomenon in the radiation belts that has been a topic of interest in the space physics community is wave-particle interactions that, as we will explore throughout this dissertation, can accelerate particles to very high energies (e.g. $\approx$ MeV for electrons) and scatter them into the atmosphere.

The goal of this dissertation is to study the wave-particle scattering mechanism that scatters electron microbursts. Electron microbursts, henceforth referred to as microbursts, are typically observed by low Earth orbiting spacecraft, sounding rockets, and high altitude balloons as a sub-second impulse of electrons. Some of the most intense microbursts are observed as a 10 to 100 fold increase of electrons (for example see Fig. 7 in Blake et al. (1996)). Since they were first reported by Anderson and Milton (1964), the short microburst duration and their impulsive nature have compelled countless researchers to understand their properties and the physical mechanism(s) that create microbursts. Microbursts are widely believed to be created by wave-particle scattering between a plasma wave called whistler mode chorus and outer radiation belt electrons, although many details regarding the scattering mechanism are unconstrained or unknown.

This chapter serves as an introduction to the physics of charged particles, plasma waves, and the wave-particle interactions in Earth's magnetosphere. We will first derive the motion of individual charged particles in Earth's electric and magnetic fields. Then we will cover how various groups of charged particles coalesce to form the major particle populations in the magnetosphere. Then, we will cover the various mechanisms that accelerate particles in the magnetosphere. Lastly, we will review the basics of microbursts as a jumping-off point for the rest of the dissertation.

Charged Particle Motion in Electric and Magnetic Fields

A charged particle trapped in the magnetosphere will experience three types of periodic motion in Earth's nearly dipolar magnetic field. The three motions are ultimately due to the Lorentz force that a particle of momentum $\vec{p}$, charge q, and velocity $\vec{v}$ experiences in an electric field $\vec{E}$ and magnetic field $\vec{B}$ and is given by

$$\frac{d\vec{p}}{dt} = q(\vec{E} + \vec{v} \times \vec{B}). \tag{1.1}$$

In the magnetosphere, the three periodic motions, in decreasing frequency, are gyration, bounce, and drift and are schematically shown in Fig. 1.1. Each of periodic these motions have a corresponding conserved quantity i.e. an adiabatic invariant.

The highest frequency periodic motion is gyration about a magnetic field of magnitude B. This motion is circular with a Larmor radius of

$$r = \frac{mv_\perp}{|q|B} \tag{1.2}$$

where m is the mass and $v_\perp$ the particle's velocity perpendicular to $\vec{B}$. This motion

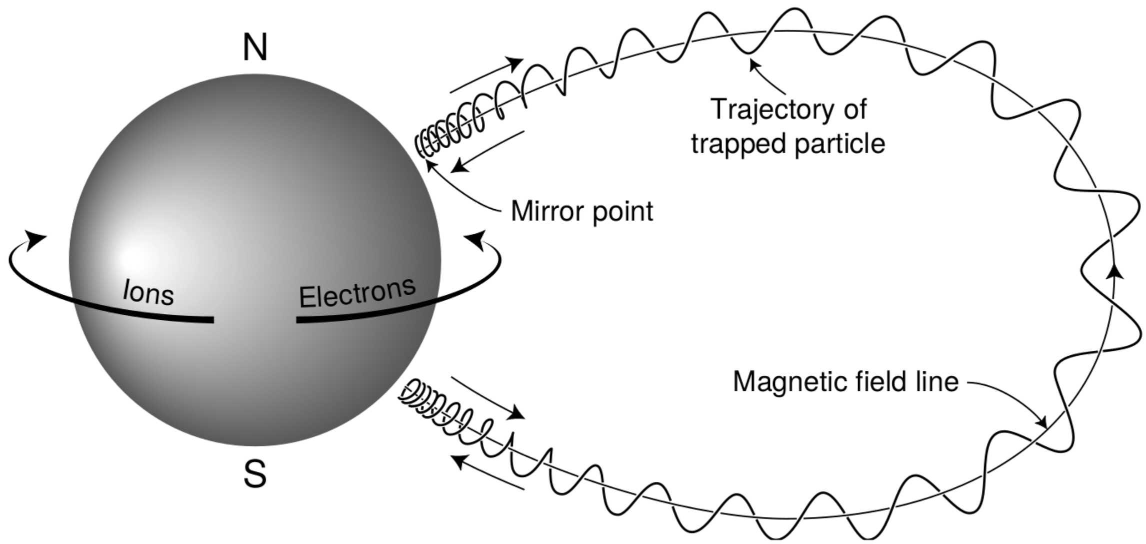

Figure 1.1: The three periodic motions of charged particles in Earth's dipole magnetic field. These motions are: gyration about the magnetic field line, bounce motion between the magnetic poles, and azimuthal drift around the Earth. Figure from (Baumjohann and Treumann, 1997).

has a corresponding gyrofrequency

$$\Omega = \frac{|q|B}{m} \tag{1.3}$$

in units of radians/second. Inside the radiation belts the electron gyrofrequency, Ω_e is on the order of a kHz. The corresponding adiabatic invariant is found by integrating the particle's canonical momentum around the particle's path of gyration

$$J_i = \oint (\vec{p} + q\vec{A}) \cdot d\vec{l} \tag{1.4}$$

where J_i is the i^{th} adiabatic invariant and $\vec{A}$ is the magnetic vector potential. This integral is carried out by integrating the first term over the circumference of the gyro orbit and integrating the second term using Stokes theorem to calculate the magnetic flux enclosed by the gyro orbit. The gyration invariant is then $J_1 \sim v_\perp^2/B$, which is conserved when the frequency, ω of a force acting on the gyrating electron satisfies $\omega << \Omega_e$.

The second highest frequency periodic motion is bouncing due to a parallel gradient in $\vec{B}$. This periodic motion naturally arises in the magnetosphere because Earth's magnetic field is stronger near the poles, and artificially in the laboratory in magnetic bottle machines. To understand this motion we first we need to define the concept of pitch angle α as the angle between $\vec{B}$ and $\vec{v}$ which is schematically shown in Fig. 1.2a. The pitch angle relates v with $v_\perp$, and $v_{||}$ (the component of the particles velocity parallel to $\vec{B}$). As shown in 1.2b and c, a smaller (larger) α will increase (decrease) the distance that the charged particle travels parallel to $\vec{B}$, during one gyration.

Assuming the particle's kinetic energy is conserved, the conservation of J_1 implies that given a particle's $v_\perp(0)$ and $B(0)$ at the magnetic equator (where Earth's magnetic field is usually at a minimum), we can calculate its $v_\perp(s)$ along the particle's path s by calculating $B(s)$ from magnetic field models. The particle's perpendicular velocity is then related via

$$\frac{v_\perp^2(0)}{B(0)} = \frac{v_\perp^2(s)}{B(s)} \tag{1.5}$$

which can be rewritten as

$$\frac{v^2 \sin^2 \alpha(0)}{B(0)} = \frac{v^2 - v_{||}^2(s)}{B(s)} \tag{1.6}$$

and re-arranged to solve for $v_{||}(s)$

$$v_{||}(s) = v\sqrt{1 - \frac{B(s)}{B(0)} \sin^2 \alpha(0)} \tag{1.7}$$

which will tend towards 0 when the second term in the radical approaches 1.

The location where $v_{||}(s) = 0$ is called the mirror point and is where a particle reverses direction. Since Earth's magnetic field is stronger towards the poles, the mirroring particle will execute periodic bounce motion between its two mirror points in the northern and southern hemispheres. The corresponding adiabatic invariant, J_2 is

$$J_2 = \oint p_{||} ds \tag{1.8}$$

where ds describes the particle path between the mirror points in the northern and southern hemispheres (see Fig. 1.1). J_2 is found by substituting Eq. 1.7 into Eq. 1.8 and defining the magnetic field strength at the mirror points as B_m where $\alpha(m) = 90°$. The J_2 integral can be written as

$$J_2 = 2p \int_{m_n}^{m_s} \sqrt{1 - \frac{B(s)}{B(m)}} ds \tag{1.9}$$

where m_n and m_s are the northern and southern mirror points, respectively. The bounce period can be estimated (e.g. Baumjohann and Treumann, 1997) to be

$$t_b \approx \frac{LR_e}{\sqrt{W/m}}(3.7 - 1.6 \sin\alpha(0)) \tag{1.10}$$

where L is the L-shell which describes the distance from the Earth's center to the location where a particular magnetic field line crosses the magnetic equator, in units of Earth radii, R_e. W is the particle's kinetic energy. As with gyration, the particle will bounce between the mirror points as long as $\omega << \Omega_b$, where Ω_b is the bounce frequency.

At this stage it is instructional to introduce the notion of the loss cone pitch angle, α_L. A particle with $\alpha \leq \alpha_L$ will mirror at or below $\approx$ 100 km altitude in

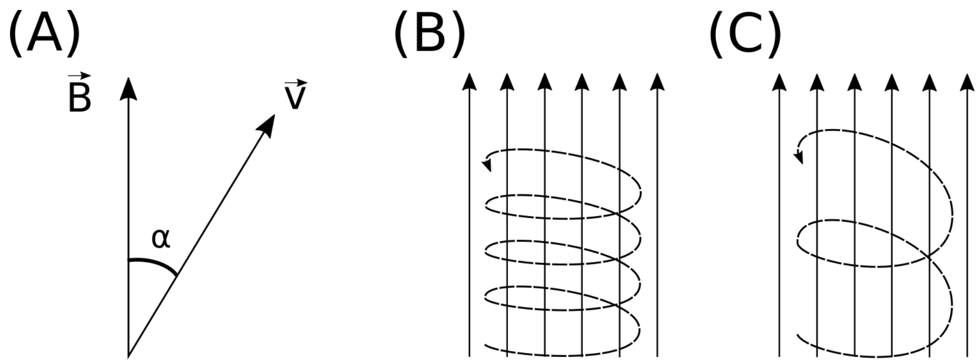

Figure 1.2: Charged particle motion in a uniform magnetic field $\vec{B}$. Panel (A) shows the geometry defining the pitch angle, α. Panel (B) and (C) show two helical electron trajectories with dashed lines assuming a large and small α (corresponding to a small and large parallel velocity $v_{||}$), respectively.

the atmosphere. A charged particle gyrating at those altitudes will encounter and Coulomb scatter with the dense atmosphere and be lost from the magnetosphere.

The slowest periodic motion experienced by charged particles in Earth's magnetic field is azimuthal drift around the Earth. This drift results from a combination of a radial gradient in $\vec{B}$ and the curvature of the magnetic field. The radial gradient drift arises because Earth's magnetic field is stronger near the Earth where the particle's gyroradius radius of curvature is smaller as it gyrates towards stronger magnetic field, and larger when it gyrates outward. The overall effect is the particle gyro orbit does not close on itself and negatively charged particles drift east and positively charged particles drift west. The radial gradient drift is enhanced by the centrifugal force that a particle experiences as it bounces along the curved field lines. The drift adiabatic invariant, J_3 is found by integrating Eq. 1.4 over the complete particle orbit around the Earth. The shape of this drift orbit is otherwise known as a drift shell. For J_3, the first term is negligible and the second term is the magnetic flux enclosed by the drift shell, Φ_m i.e. $J_3 \sim \Phi_m$.

Figure 1.3 from Schulz and Lanzerotti (1974) shows contours of the gyration, bounce, and drift frequencies for electrons and protons in Earth's dipole magnetic field.

Up until now we have considered the three periodic motions due Earth's magnetic field and the absence of electric fields. If $\vec{E}$ is present, a particle's center of gyration i.e., averaged position of the particle over a gyration, will drift with a velocity perpendicular to both $\vec{E}$ and $\vec{B}$. The drift velocity can be solved directly from Eq. 1.1 and is

$$\vec{v}_E = \frac{\vec{E} \times \vec{B}}{B^2}. \tag{1.11}$$

Lastly, for more detailed derivations of these motions, see the following texts: Baumjohann and Treumann (1997); Schulz and Lanzerotti (1974); Tsurutani and Lakhina (1997).

Particle Populations and Their Interractions in the Magnetosphere

Now that we have looked at the dynamics of single-particle motion in electric and magnetic fields, we will briefly tour the various macroscopic populations in the magnetosphere that are illustrated in Fig. 1.4.

The sun and its solar wind are ultimately the source of energy input into the magnetosphere. The solar wind at Earth's orbit is a plasma traveling at supersonic speeds with an embedded interplanetary magnetic field (IMF). When the solar wind encounters Earth's magnetic field, the plasma can not easily penetrate into the magnetosphere because the plasma is frozen-in on magnetic field lines. Thus the plasma and its magnetic field drapes around the magnetosphere forming a cavity in the solar wind that is roughly shaped as shown in Fig. 1.4. Because the solar wind is supersonic at 1 AU, a bow shock exists upstream of the magnetosphere. The solar wind plasma, after it is shocked by the bow shock, flows around the magnetosphere

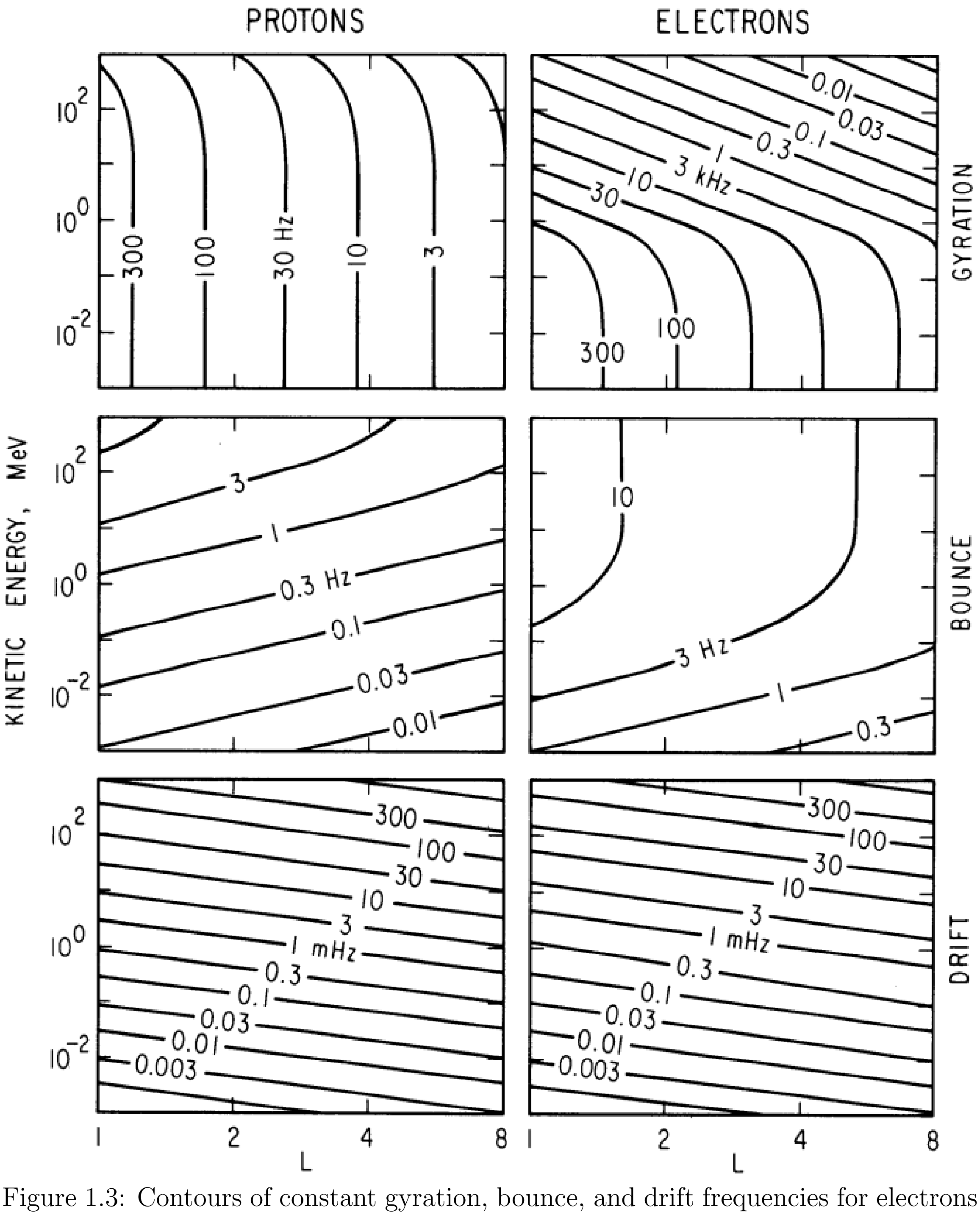

Figure 1.3: Contours of constant gyration, bounce, and drift frequencies for electrons and protons in a dipole field. Figure from Schulz and Lanzerotti (1974).

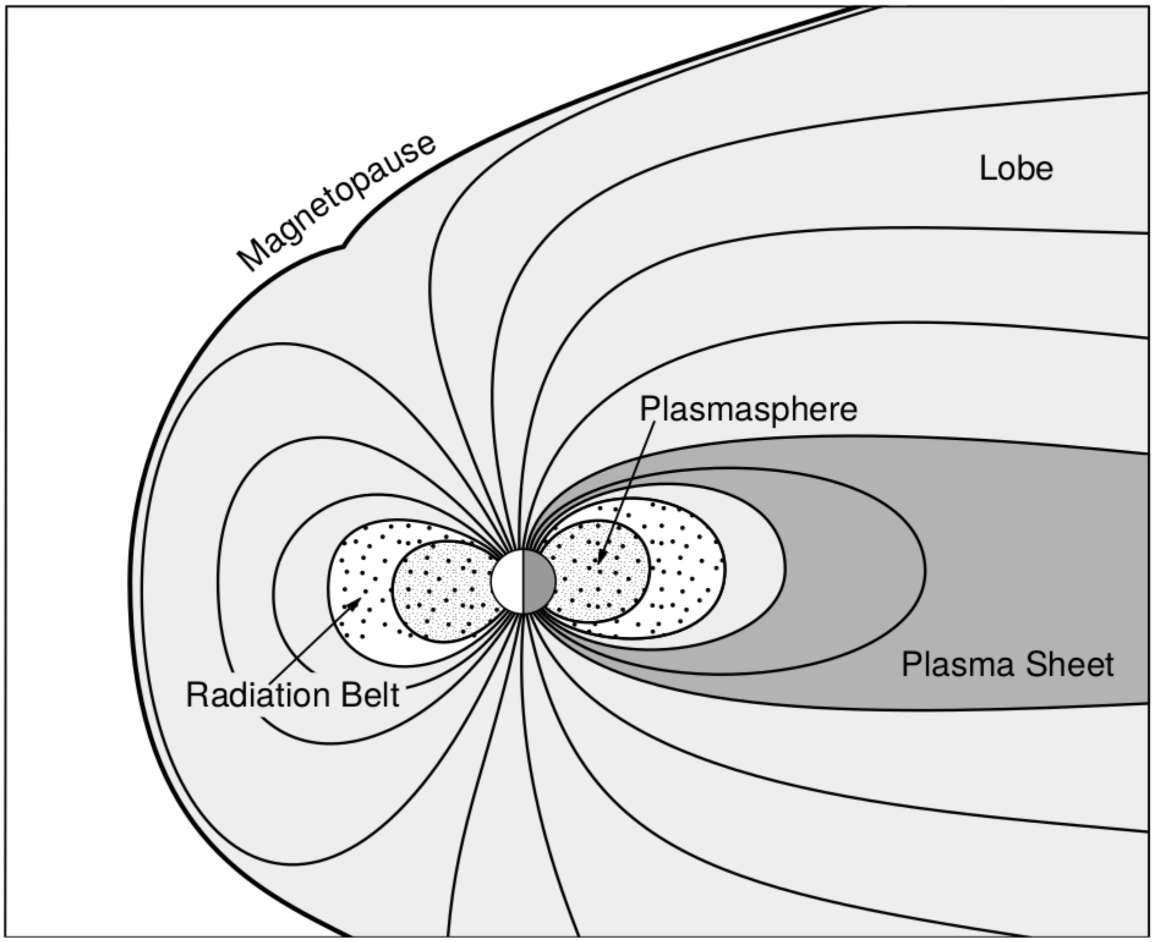

Figure 1.4: Macroscopic structures in the inner magnetosphere most relevant to this dissertation. The plasmasphere, and the radiation belts are shown and ring current is co-located there as well. Figure from Baumjohann and Treumann (1997).

inside the magnetosheath. The surface where the solar wind ram pressure and Earth's magnetic pressure balance is termed the magnetopause, which can be thought of as a boundary between the solar wind's and Earth's plasma environments. This is a slightly naive description of the magnetopause, but is nonetheless an instructive conceptual picture. The shocked plasma then flows past the Earth where it shapes the magnetotail. In the magnetotail the solar wind magnetic pressure balances Earth's magnetic field pressure in the lobes. The magnetotail extends on the order of 100 R_E downstream of Earth, and the tailward stretching of magnetic field lines creates the plasma sheet which exists in the region of low magnetic field strength near the magnetic equator (e.g. Eastwood et al., 2015).

Populations in the Inner Magnetosphere

Closer to Earth, where the magnetic field is largely dipolar, are three plasma populations that comprise the inner magnetosphere: the plasmasphere, the ring current, and the radiation belts. Before we describe these three particle populations in detail, we will first introduce the coordinate system that most naturally describes the inner magnetosphere environment, and the electric fields that affect mostly low energy particles.

In this coordinate system the "radial" coordinate was defined in section 1 and is the L shell. The azimuthal coordinate is the magnetic local time (MLT). For an observer above Earth's north pole looking down, MLT is defined to be 0 (midnight) in the anti-sunward direction, and increases in the counter-clockwise direction with 6 at dawn, 12 at noon (sunward direction), and 18 in dusk. The final coordinate is the magnetic latitude, λ which is analogous to the latitude coordinate in the spherical coordinate system, and is defined to be 0 at the magnetic equator. This coordinate system naturally describes the following inner magnetosphere populations.

The low energy particle dynamics in the inner magnetosphere are organized by two electric fields: the co-rotation and the dawn-dusk electric fields. The co-rotation electric field arises from the rotation of Earth's magnetic field. Since particles are frozen on magnetic field lines and the plasma conductivity is effectively infinite, to a non-rotating observer, Earth's rotation appears as a radial electric field that drops off as $\sim L^2$. This electric field makes particles orbit around the Earth due to the $\vec{E} \times \vec{B}$ drift. The other electric field, pointing from dawn to dusk is called the convection electric field and is due to the Earthward transport of particles from the magnetotail that appears as an electric field to a stationary observer (with respect to Earth). The superposition of the co-rotation and and convection electric fields results in a potential field shown in Fig. 1.5. The shaded area in Fig. 1.5 shows the orbits on which low energy electrons are trapped, and outside are the untrapped particles. The dynamic topology of the shaded region in Fig. 1.5 is controlled by only the convection electric field which is dependent on the solar wind speed and the IMF. The lowest energy particles, that are most effected by these electric fields, make up the plasmasphere.

Plasmasphere The plasmasphere is a dense ($n_e \sim 10^3/\text{cm}^3$), cool plasma ($\sim$ eV) that extends to $L \sim 4$ (extent is highly dependent on the solar wind and magnetospheric conditions) and is sourced from the ionosphere. The two main mechanisms that source the cold plasma from the ionosphere are ultraviolet ionization by sunlight and particle precipitation. The ultraviolet ionization by sunlight is strongly dependent on the time of day (day vs night), latitude (more ionization near the equator). The ionization due to particle precipitation, on the other hand, is highly dependent on magnetospheric conditions, and mostly occurs at high latitudes.

The outer boundary of the plasmasphere is the plasmapause which is typically identified as a steep radial gradient in plasma density from $\sim 10^3/\text{cm}^3$ to $\sim 1/\text{cm}^3$. As

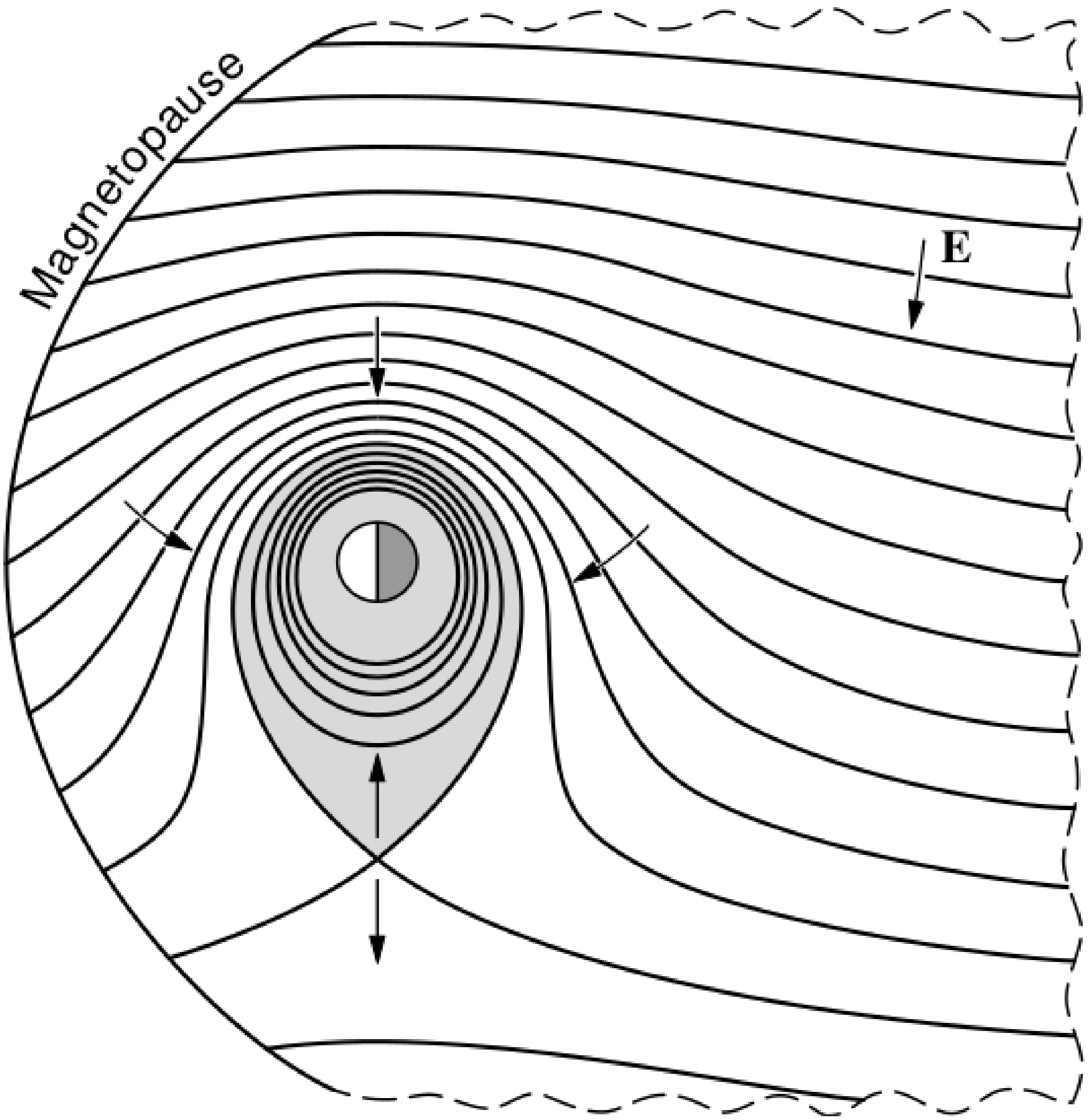

Figure 1.5: Equipotential lines and electric field arrows due to the superposition of the co-rotation and convection electric fields. Electrons in the shaded region execute closed orbits. Outside of the shaded regions the electrons are not trapped and will escape. The region separating the two regimes is called the Alfven layer. Figure from Baumjohann and Treumann (1997).

we will see throughout this dissertation, the location of the plasmapause is important to model (e.g. O'Brien and Moldwin, 2003) and understand since the plasma density strongly controls the efficiency of particle scattering (Horne et al., 2005).

Ring Current The next higher energy population is the ring current. This population consists of protons and electrons between tens and a few hundred keV that drift around the Earth. The orbits of higher energy particles are not as effected by the convection and co-rotation electric field, rather they drift around the Earth due to gradient and curvature drifts. Since the direction of the drift is dependent on charge, protons drift west around the Earth and electrons drift East. This has the effect of creating a current around the Earth.

The ring current generates a magnetic field which decreases the magnetic field strength on Earth's surface and increases it outside of the ring current. The decrease of Earth's magnetic field strength is readily observed by a system of ground-based magnetometers and is merged into a Disturbance Storm Time (DST) index. An example of a DST index time series from a coronal mass ejection (CME) driven 2015 St. Patrick's Day storm is shown in Fig. 1.6. The ring current is sometimes first depleted and DST increases slightly (initial phase or sudden storm commencement). Then the ring current is rapidly built up during which DST rapidly decreases (main phase). Lastly the ring current gradually decays toward its equilibrium state over a period of a few days and DST increases towards 0 (recovery phase). The DST index along with other indicies are readily used by the space physics community to quantify the global state of the magnetosphere.

Radiation Belts The highest energy particle populations are in the Van Allen radiation belts. These belts were discovered by Van Allen (1959) and Vernov and Chudakov (1960) during the Cold War and are a pair of toroidally shaped populations

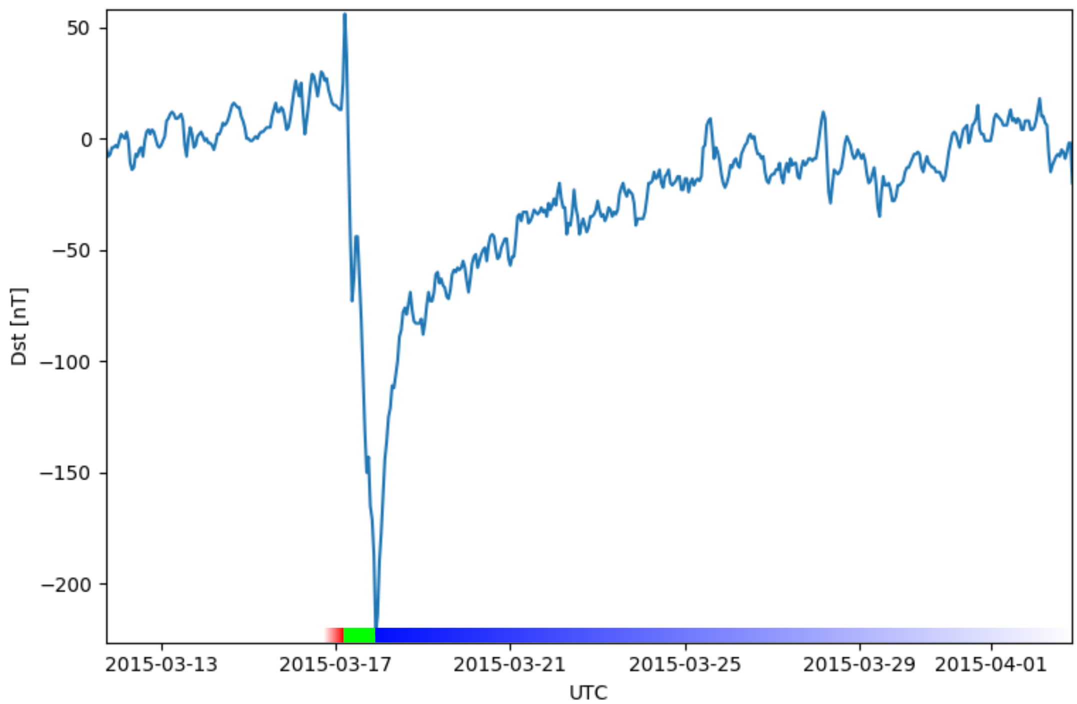

Figure 1.6: The DST index during the St. Patrick's Day 2015 storm. This storm was caused by a coronal mass ejection on March 15th, 2015. The storm phases are: initial phase, main phase, and recovery phase. The initial phase occurred when the Dst peaked at +50 nT on March 17th during which the ring current was eroded by the coronal mass ejection during the interval shown by the red bar. Then the rapid decrease to ≈ -200 nT was during the main phase where many injections from the magnetotail pumped up the ring current which reduced Earth's magnetic field strength at the ground and is shown with the green bar. Lastly, the recovery phase lasted from March 18th to approximately March 29th during which the ring current particles were lost and the ring current returned to its equilibrium state. The recovery phase is shown with the blue bar.

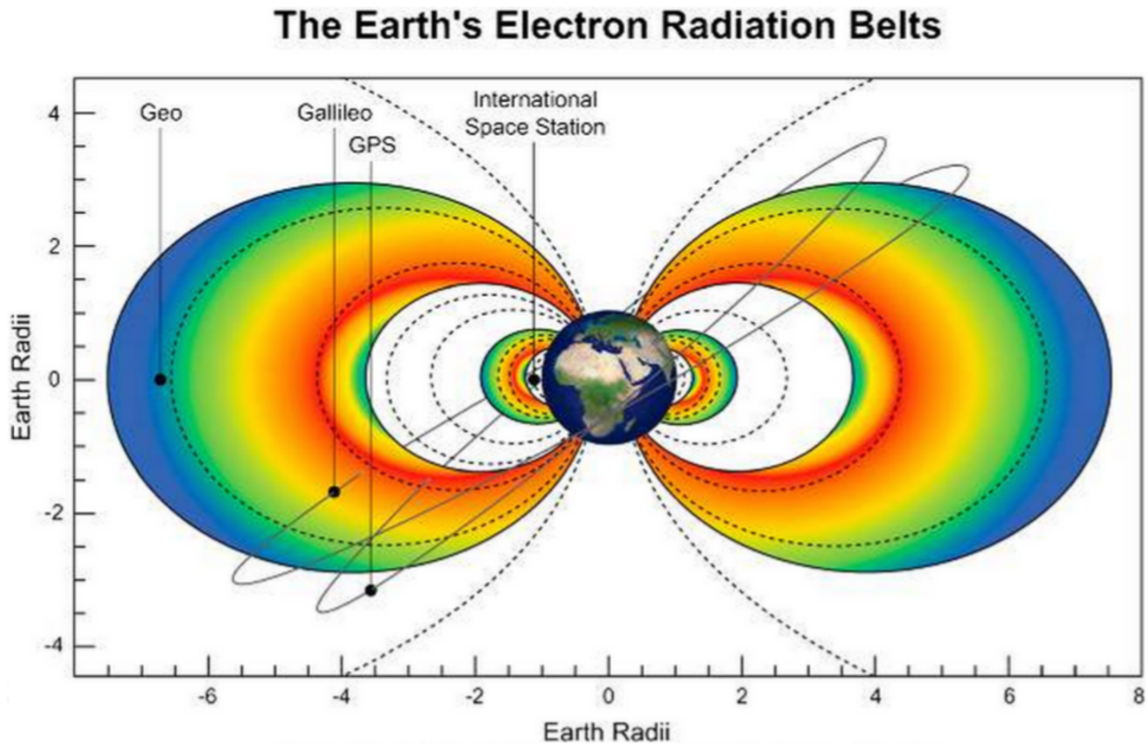

Figure 1.7: The two radiation belts with a the locations of various satelites and orbits. Figure from (Horne et al., 2013).

of trapped electrons and protons usually within to $L < 8$ and are shown in Fig. 1.7. Their quiescent toroidal shape is similar to the shape of the plasmasphere and ring current and is a result of Earth's dipole magnetic field and the conservation of the three adiabatic invariants discussed in section 1.

The inner radiation belt is extremely stable on time periods of years, extends to $L \approx 2$, and mainly consists of protons with energies between MeV and GeV and electrons with energies up to ≈ 1 MeV (Claudepierre et al., 2019). The source of inner radiation belt protons is believed to be due to cosmic-ray albedo neutron decay (e.g. Li et al., 2017) and inward radial diffusion for electrons (e.g. O'Brien et al., 2016). The gap between the inner and outer radiation belt is called the slot, which is believed to be due to hiss waves inside the plasmasphere (described below) scattering

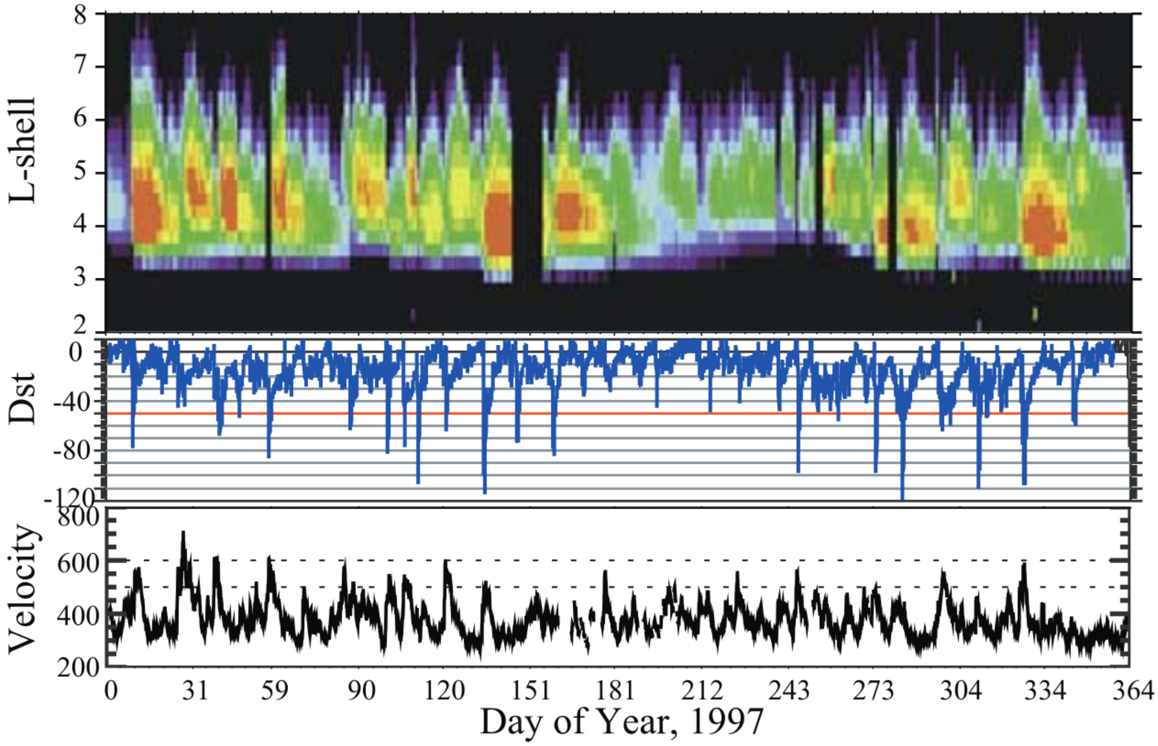

Figure 1.8: The dynamics of the outer radiation belt in 1997 from the POLAR satellite. Top panel shows the 1.2-2.4 MeV electron flux as a function of L and 1997 day of year. The middle panel shows the DST index, and bottom panel shows the solar wind velocity. Figure from (Reeves et al., 2003).

particles into the atmosphere (e.g. Breneman et al., 2015; Lyons and Thorne, 1973).

The outer radiation belt, on the other hand is much more dynamic and consists of mainly electrons of energies up to a few MeV. The outer belt's spatial extent is highly variable e.g. see Fig. 1.8, and is typically observed at $4 < L < 8$. Since the outer radiation belt contains a dynamic population of energetic particles that pose a threat to human and technological presence in Earth's atmosphere and space, decades of research has been undertaken to understand and predict the outer radiation belt particles, waves, and wave-particle interactions. The dynamics of the outer radiation belt can be understood by considering various competing acceleration and loss mechanisms which will be described in the following sections.

Radiation Belt Particle Sources and Sinks

Adiabatic Heating

One of the particle heating and transport mechanisms arises from the Earthward convection of particles. The conservation of J_1 implies that the initial and final $v_\perp$ depends on the change in the magnetic field amplitude

$$\frac{v_{\perp\ i}^2}{B_i} = \frac{v_{\perp\ f}^2}{B_f}. \tag{1.12}$$

As a particle convents Earthward, $B_f > B_i$ thus $v_\perp$ must increase. The dipole magnetic field amplitude can be written as

$$B(L,\theta) = \frac{31.2\ \mu\mathrm{T}}{L^3}\sqrt{1 + 3\cos^2\theta} \tag{1.13}$$

which implies that

$$\frac{v_{\perp\ f}^2}{v_{\perp\ i}^2} = \left(\frac{L_i}{L_f}\right)^3. \tag{1.14}$$

.

In addition, as the particle convects Earthward the distance between the particle's mirror points decrease. If J_2 is conserved, the shrinking bounce path implies that $v_{||}$ must increase by

$$\frac{v_{||\ f}^2}{v_{||\ i}^2} = \left(\frac{L_i}{L_f}\right)^k \tag{1.15}$$

where k ranges from 2 for equatorial pitch angles, $\alpha_{eq} = 0°$, to 2.5 for $\alpha_{eq} = 90°$ (Baumjohann and Treumann, 1997). Since the rate of adiabatic heating is greater in the perpendicular direction than heating in the parallel direction, an initially isotropic particle distribution will become anisotropic during its convection. These isotropic particles can then become unstable to wave growth and generate waves in order to reach equilibrium.

Wave Resonance Heating

Another mechanism that heats particles is due to particles resonating with plasma waves. A few of the electromagnetic wave modes responsible for particle acceleration (and deceleration) relevant to radiation belt dynamics are hiss, whistler mode chorus (chorus), and electromagnetic ion cyclotron (EMIC) waves. These waves are created by the loss cone instability that driven by an anisotropy of electrons for chorus waves, and protons for EMIC waves. The level of anisotropy can be quantified by the ratio of the perpendicular to parallel particle temperatures ($T_{\perp}/T_{||}$). A particle distribution is unstable when $T_{\perp}/T_{||} > 1$ which facilitates wave growth.

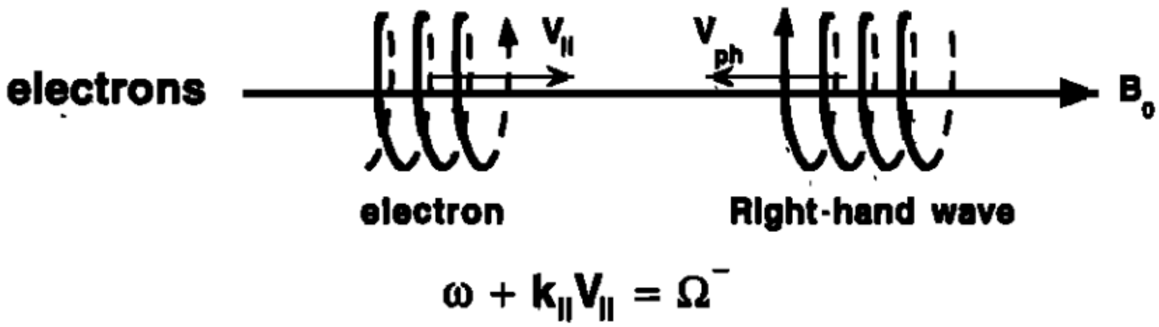

Figure 1.9: The trajectories of an electron and a right-hand circularly polarized wave during a cyclotron resonance. The electron's $v_{||}$ and the wave's $k_{||}$ are in opposite directions such that the wave's frequency is Doppler shifted to a integer multiple of the electron cyclotron frequency. Figure from (Tsurutani and Lakhina, 1997).

Since electrons gyrate in a right-handed sense, the chorus waves also tend to be right hand circularly polarized (Tsurutani and Lakhina, 1997). The same argument applies to protons and left hand circularly polarized EMIC waves as well.

These circularly polarized waves can resonate with electrons and/or protons when their combined motion results in a static $\vec{E}$. One example of a resonance between a right hand circularly polarized wave and an electron is shown in Fig. 1.21 and is termed the cyclotron resonance. An electron's $v_{||}$ and the wave's parallel wave vector, $k_{||}$ are in opposite directions such that the wave frequency ω is Doppler shifted to an integer multiple of the Ω_e at which point the electron feels a static electric field and is accelerated or decelerated. This acceleration happens when a resonance condition is satisfied between a wave and a particle for which we will now derive an illustrative toy model.

Assume a uniform magnetic field $\vec{B} = B_0\hat{z}$ with a parallel propagating ($k = k\hat{z}$), right-hand circularly polarized wave. The wave's electric field as a function of position and time can be written as

$$\vec{E} = E_0(\cos(\omega t - kz)\hat{x} + \sin(\omega t - kz)\hat{y}) \tag{1.16}$$

which is more clearly expressed by taking the dot product to find $\vec{E}$ in the $\hat{\theta}$ direction

$$E_\theta = \vec{E} \times \hat{\theta} = E_0 \cos\left(\omega t - kz + \theta\right). \tag{1.17}$$

Now assume that the electron is traveling in the $-\hat{z}$ direction with a velocity $\vec{v} = -v_0\hat{z}$ so its time dependent position along $\hat{z}$ is

$$z(t) = -v_0 t \tag{1.18}$$

and gyrophase is

$$\theta(t) = -\Omega t + \theta(0) \tag{1.19}$$

where the first negative sign comes from the electron's negative charge. Now we put this all together and express the electric field and the force that the electron will experience

$$m\frac{dv_\theta}{dt} = qE_\theta = qE_0 \sin\left((\omega + kv_0 - \Omega)t + \theta(0)\right). \tag{1.20}$$

This is a relatively complex expression, but when the time dependent component,

$$\omega + kv_0 - \Omega = 0, \tag{1.21}$$

the electron will be in a static electric field which will accelerate or decelerate the electron depending on θ_0, the phase between the wave and the electron. Show Bortnik 2008 plot? The expression in Eq. 1.21 is commonly referred to as the resonance condition and is more generally written as

$$\omega - k_{||}v_{||} = \frac{n\Omega_e}{\gamma} \tag{1.22}$$

where n is the resonance order, and γ is the relativistic correction (e.g. Millan and Thorne, 2007). In the case of the cyclotron resonance, $\omega \approx \Omega_e$ thus J_1 is violated. Since J_1 is violated, J_2 and J_3 are also violated since the conditions required to violate J_2 and J_3 are less stringent than J_1. It is important to remember that along the particle's orbit it will encounter and experience the effects of many waves along its orbit. The typical MLT extent of a handful of waves that are capable of resonating with radiation belt electrons are shown in Fig. 1.10.

Particle Losses

Now that we have seen two general mechanisms with which particles are accelerated and transported in the magnetosphere, we will now consider a few specific mechanisms with which particles are lost to the atmosphere or the solar wind. One particle loss mechanisms into the solar wind is magnetopause shadowing (e.g. Ukhorskiy et al., 2006). Particles are sometimes lost when the ring current is strengthened and Earth's magnetic field strength is increased outside of the ring current (and reduced on Earth's surface). If the time scale of the ring current strengthening is slower than a particle drift, J_3 is conserved. Then in order to conserve J_3 while the magnetic field strength is increased, the particle's drift shell must move outward to conserve the magnetic flux contained by the drift shell. Then if the particle's drift shell expands to the point that it crosses the magnetopause, the particle will be lost to the solar wind.

Another particle loss (and acceleration) mechanism is driven by ultra low frequency (ULF) waves and is called radial diffusion. Radial diffusion is the transport

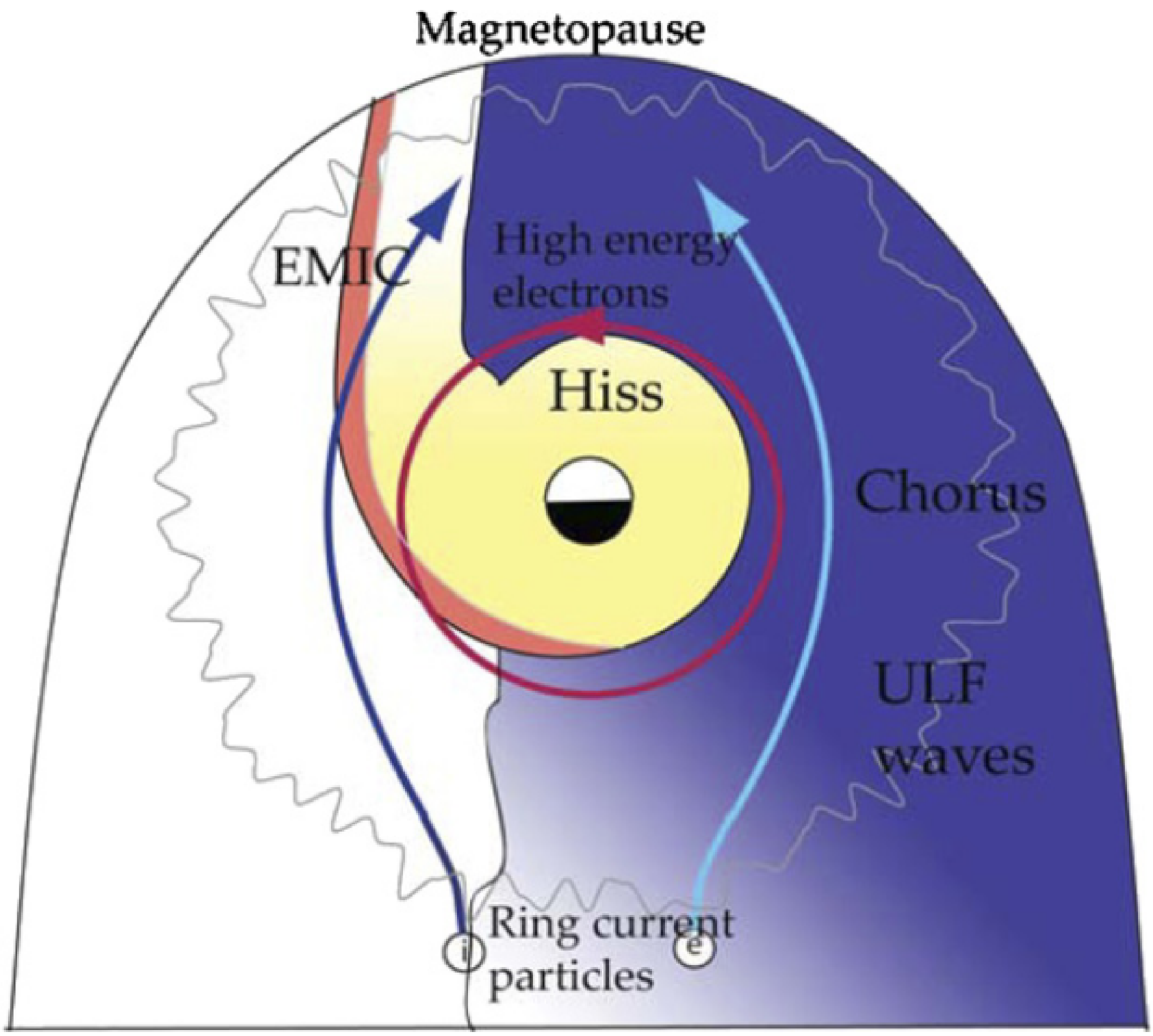

Figure 1.10: Various wave modes in the magnetosphere. Ultra low frequency waves occur throught the magnetosphere. Chorus waves are typically observed in the 0-12 midnight-dawn region. EMIC waves are typically observed in the dusk MLT sector. Hiss waves are observed inside the plasmasphere. Figure from Millan and Thorne (2007).

of particles from high to low phase space density, f. If the transport is radially inward, particles will appear to be accelerated. On the other hand, radially outward radial diffusion can transport particles through the magnetopause where they will be lost to the solar wind. Reeves et al. (2013) investigated the driver of particle acceleration during the October 2012 storm and observationally found that inward radial diffusion was not dominant, rather local acceleration via wave-resonance heating (i.e. particle diffusion in pitch angle and energy which will be described below) appeared to be the dominant acceleration mechanism.

The loss mechanism central to this dissertation is pitch angle and energy scattering of electrons by waves. Some of the waves that scatter electrons in energy and pitch angle in the inner magnetosphere are: plasmaspheric hiss (e.g. Breneman et al., 2015; O'Brien et al., 2014), EMIC waves (e.g. Capannolo et al., 2019; Hendry et al., 2017), and chorus waves (e.g. Breneman et al., 2017; Kasahara et al., 2018; Ozaki et al., 2019). These wave-particle interactions occur when the resonance condition in Eq. 1.22 is satisfied at which point the particle's energy and α is modified by the wave. More details regarding the theory of pitch angle and energy diffusion is given in Chapter X. If the wave changes α towards 0 such that $\alpha < \alpha_{LC}$, the particle's mirror point lowers to less than 100 km altitude where the particle can be lost due collisions with air. One manifestation of pitch angle scattering of particles into the loss cone are microbursts: a sub-second durtaion impulse of electrons.

Microbursts

Microbursts were first found in high altitude balloon measurements of bremsstrahlung X-rays emitted by microburst electrons impacting the atmosphere by Anderson and Milton (1964). In the following years, numerous balloon flights expanded our knowledge of non-relativistic microbursts (relativistic microbursts have not yet been observed by high altitude balloons) by quantifying the microburst spatial extent, temporal width, occurrence frequency, extent in L and MLT, and their source (a local plasma instability vs. a propagating disturbance in the magnetosphere) (e.g. Barcus et al., 1966; Brown et al., 1965; Parks, 1967; Trefall et al., 1966). Since then, non-relativistic and relativistic (> 500 keV) microbursts electrons have been directly observed in LEO with spacecraft including the Solar Anomalous and Magnetospheric Particle Explorer (SAMPEX) (e.g. Blake et al., 1996; Blum et al., 2015; Douma et al., 2019, 2017; Greeley et al., 2019; Lorentzen et al., 2001a,b; Nakamura et al., 1995, 2000; O'Brien et al., 2004, 2003), Montana State University's (MSU) Focused Investigation of Relativistic Electron Bursts: Intensity, Range, and Dynamics II (FIREBIRD-II) (Anderson et al., 2017; Breneman et al., 2017; Crew et al., 2016; Klumpar et al., 2015; Spence et al., 2012), and Science Technologies Satellite (STSAT-I) (e.g. Lee et al., 2012, 2005). An example microburst time series is shown in Fig. 1.11 and was observed by the FIREBIRD-II CubeSats. The prominent features of the example microbursts in Fig. 1.11 are their < 1 second duration, half order of magnitude increase in count rate above the falling background, and their approximately 200-800 keV energy extent.

Microbursts are observed on magnetic field footprints that are connected to the outer radiation belt (approximately $4 < L < 8$), and are predominately observed in the 0-12 MLT sector with an elevated occurrence frequency during magnetospherically disturbed times as shown in Fig. 1.12 (e.g. Douma et al., 2017). O'Brien et al. (2003) used SAMPEX relativistic electron data and found that microbursts predominately occur during the main phase of storms, with a heightened occurrence rate during the recovery phase. Microburst occurrence rates also appear to be higher during high solar wind velocity events e.g. from co-rotating interaction regions (Greeley et al., 2019; O'Brien et al., 2003).

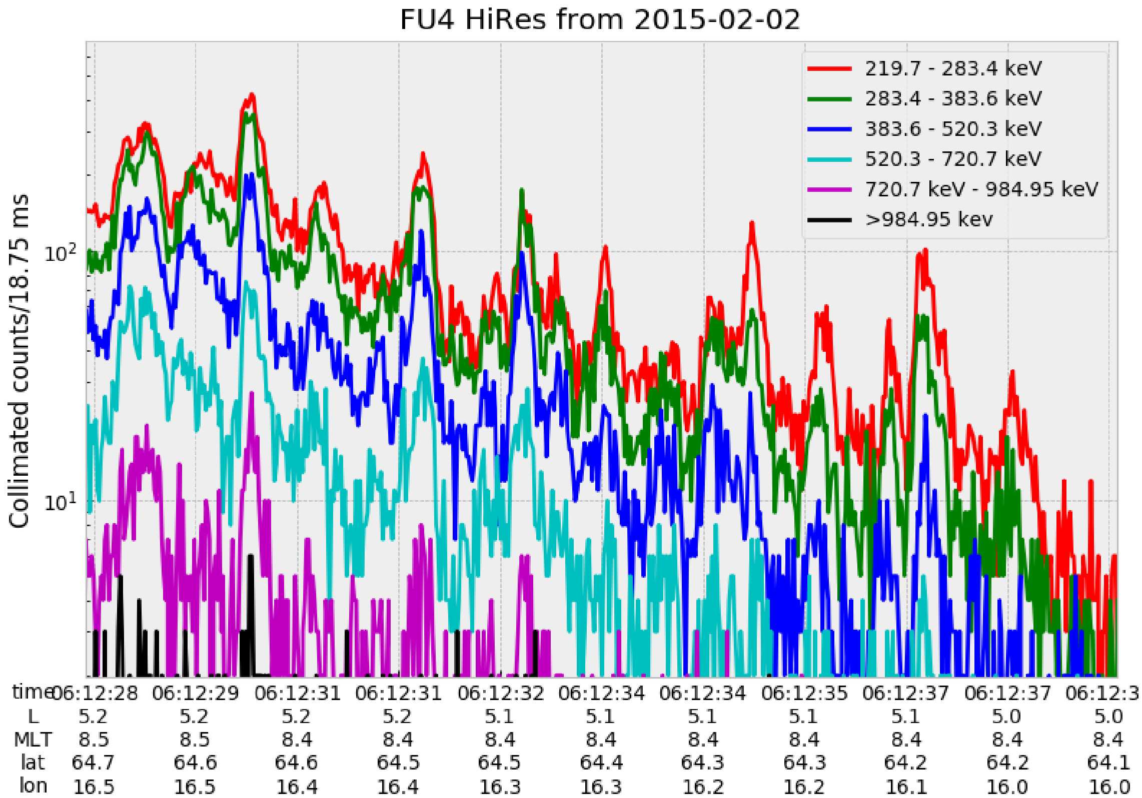

Figure 1.11: An example train of microbursts observed by FIREBIRD-II unit 4 on February 2nd, 2015. The colored curves show the differential energy channel count rates in six channels from ≈ 200 keV to greater than 1 MeV. The x-axis labels show auxiliary information such as time of observation and the spacecraft position in L, MLT, latitude and longitude coordinates.

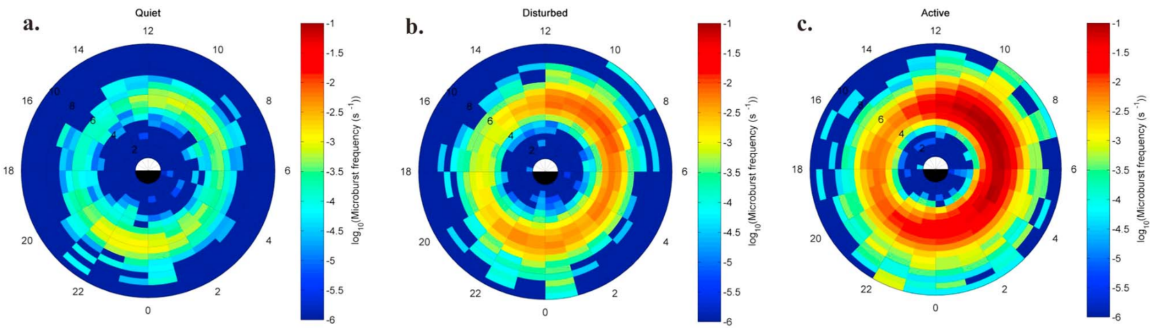

Figure 1.12: Relativistic (> 1MeV) distribution of microburst occurrence rates as a function of L and MLT. The three panels show the microburst occurrence rate dependence on geomagnetic activity, parameterized by the auroral electrojet (AE) index for (a) AE $<$ 100 nT, (b) 100 $<$ AE $<$ 300 nT and (c) AE $>$ 300 nT. Figure from Douma et al. (2017).

The impact of microbursts on atmospheric chemistry has been estimated to be significant. Relativistic microburst electrons impacting the atmosphere are ionized at $<$ 100 km altitudes, with higher energy electrons penetrating closer to the surface. The resulting chemical reaction of microburst electrons impacting the atmosphere produces odd hydrogen HO_x and odd nitrogen NO_x molecules. These molecules are partially responsible for destroying ozone (O_3). Seppälä et al. (2018) modeled a six hour relativistic microburst storm and found that the mesospheric ozone was reduced by $7 - 12\%$ in the summer months and $12 - 20\%$ in the winter months.

Furthermore, microbursts have also been estimated to have a significant impact on the outer radiation belt electrons. Radiation belt electron loss due to microbursts has been estimated to be on the on the order of a day (Breneman et al., 2017; Douma et al., 2019; Lorentzen et al., 2001b; O'Brien et al., 2004; Thorne et al., 2005).

The wave-particle interactions responsible for generating microbursts are also believed to accelerate electrons in the radiation belts. As mentioned earlier, when an electron is in resonance with a wave, energy is exchanged with the wave and the electron is either accelerated or decelerated. The signature of wave-particle acceleration been observed for radiation belt electrons (e.g. Horne et al., 2005; Meredith et al., 2002; Reeves et al., 2013). O'Brien et al. (2003) presented evidence that enhancements in chorus waves, microbursts, and radiation belt electrons are related. O'Brien et al. (2003) proposed an explanation where microburst precipitation is a side effect of electron acceleration due to chorus waves. The widely used theoretical framework to model interactions between electrons and chorus waves is quasi-linear diffusion (e.g. Horne et al., 2005; Meredith et al., 2002; Summers, 2005; Summers et al., 1998; Thorne et al., 2005; Walker, 1993) which is derived in Chapter **??**. Qualitatively, when a particle is resonant with a wave it can be transported in pitch angle towards the loss cone and lose energy to the wave. In contrast, if the particle is transported away from the loss cone, it gains energy from the wave.

The range of observed microburst energies range from a few tens of keV (e.g Datta et al., 1997; Parks, 1967) to greater than 1 MeV (e.g. Blake et al., 1996; Greeley et al., 2019). The microburst electron flux (J) falls off in energy, and the microburst energy spectra is typically well fit to a decaying exponential

$$J(E) = J_0 e^{-E/E_0} \tag{1.23}$$

where J_0 is the flux at 0 keV (unphysical free parameter) and E_0 quantifies the efficiency of the scattering mechanism in energy (.e.g Datta et al., 1997; Lee et al., 2005; Parks, 1967). A small E_0 suggests that mostly low energy particles are scattered and a high E_0 suggests that the scattering mechanism scatters low and high energy electrons. Reality is a bit more messy and a high E_0 may be a signature of a scattering mechanism preferential to high energy electrons, but is hidden by the convolution of the source particles available to be scattered (typically with a falling energy spectrum) and the energy-dependent scattering efficiency.

The short duration of microbursts observed by a single LEO satellite has an ambiguity when interpreting what is exactly a microburst. The two possible realities are: a microburst is very small and spatially stationary so that the LEO spacecraft passes through it in less than a second. Alternatively, microbursts are spatially large with a short duration such that the microburst passes by the spacecraft in a fraction of a second. There are a few ways to distinguish between the two possible realities, and each one has a unique set of advantages.

A high altitude balloon provides essentially a stationary view of the precipitating particles under the radiation belt footprints so a short-lived, temporal microburst can be unambiguously identified. Spatial structures, on the other hand, are difficult to identify because a balloon is essentially still on drift timescales.

Multi-spacecraft missions are an alternate solution which can determine if a microburst-like feature is spatial or temporal. As will be shown in this dissertation, if a microburst is observed simultaneously by two spacecraft then it is temporal and has a size greater than the spacecraft separation. On the contrary, if two spacecraft observe a microburst-like feature at different times, but at the same location, then the feature is spatial and may be a curtain (Blake and O'Brien, 2016). Both balloon and multi-spacecraft observational methods have a unique set of strengths, and this dissertation takes the multi-spacecraft approach to identify and study microbursts.

Scope of Reserach

This dissertation furthers our understanding of the microburst scattering mechanism by observing the scattering directly, and measuring the microburst sizes and comparing them to the size of waves near the magnetic equator where those electrons could have been scattered. Chapter **??** describes a microburst scattering event observed by NASA's Van Allen Probes which was studied in the theoretic framework of pitch angle and energy diffusion. The following two chapters will then study the size of microbursts. Chapter **??** describes a bouncing packet microburst observation made by MSU's FIREBIRD-II mission where the microburst's lower bound longitudinal and latitudinal sizes were estimated. Then Chapter **??** expands the case study from Ch. **??** to a statistical study of microburst sizes using The Aerospace Corporation's AeroCube-6 (AC6) CubeSats. In this study, a Monte Carlo and analytic microburst size models were developed to account for the compounding effects of random microburst sizes and locations. Lastly, Chapter **??** will summarize the dissertation work and make concluding remarks regarding outstanding questions in microburst physics.

Bibliography

Anderson, B., Shekhar, S., Millan, R., Crew, A., Spence, H., Klumpar, D., Blake, J., O'Brien, T., and Turner, D. (2017). Spatial scale and duration of one microburst region on 13 August 2015. *Journal of Geophysical Research: Space Physics*.

Anderson, K. A. and Milton, D. W. (1964). Balloon observations of X rays in the auroral zone: 3. High time resolution studies. *Journal of Geophysical Research*, 69(21):4457–4479.

Barcus, J., Brown, R., and Rosenberg, T. (1966). Spatial and temporal character of fast variations in auroral-zone x rays. *Journal of Geophysical Research*, 71(1):125–141.

Baumjohann, W. and Treumann, R. A. (1997). *Basic space plasma physics*. World Scientific.

Blake, J., Looper, M., Baker, D., Nakamura, R., Klecker, B., and Hovestadt, D. (1996). New high temporal and spatial resolution measurements by sampex of the precipitation of relativistic electrons. *Advances in Space Research*, 18(8):171 – 186.

Blake, J. B. and O'Brien, T. P. (2016). Observations of small-scale latitudinal structure in energetic electron precipitation. *Journal of Geophysical Research: Space Physics*, 121(4):3031–3035. 2015JA021815.

Blum, L., Li, X., and Denton, M. (2015). Rapid MeV electron precipitation as observed by SAMPEX/HILT during high-speed stream-driven storms. *Journal of Geophysical Research: Space Physics*, 120(5):3783–3794. 2014JA020633.

Breneman, A., Crew, A., Sample, J., Klumpar, D., Johnson, A., Agapitov, O., Shumko, M., Turner, D., Santolik, O., Wygant, J., et al. (2017). Observations directly linking relativistic electron microbursts to whistler mode chorus: Van allen probes and FIREBIRD II. *Geophysical Research Letters*.

Breneman, A. W., Halford, A., Millan, R., McCarthy, M., Fennell, J., Sample, J., Woodger, L., Hospodarsky, G., Wygant, J. R., Cattell, C. A., et al. (2015). Global-scale coherence modulation of radiation-belt electron loss from plasmaspheric hiss. *Nature*, 523(7559):193.

Brown, R., Barcus, J., and Parsons, N. (1965). Balloon observations of auroral zone x rays in conjugate regions. 2. microbursts and pulsations. *Journal of Geophysical Research (U.S.)*.

Capannolo, L., Li, W., Ma, Q., Shen, X.-C., Zhang, X.-J., Redmon, R., Rodriguez, J., Engebretson, M., Kletzing, C., Kurth, W., et al. (2019). Energetic electron precipitation: multi-event analysis of its spatial extent during emic wave activity. *Journal of Geophysical Research: Space Physics*.

Claudepierre, S., O'Brien, T., Looper, M., Blake, J., Fennell, J., Roeder, J., Clemmons, J., Mazur, J., Turner, D., Reeves, G., et al. (2019). A revised look at relativistic electrons in the earth's inner radiation zone and slot region. *Journal of Geophysical Research: Space Physics*, 124(2):934–951.

Crew, A. B., Spence, H. E., Blake, J. B., Klumpar, D. M., Larsen, B. A., O'Brien, T. P., Driscoll, S., Handley, M., Legere, J., Longworth, S., Mashburn, K., Mosleh, E., Ryhajlo, N., Smith, S., Springer, L., and Widholm, M. (2016). First multipoint in situ observations of electron microbursts: Initial results from the NSF FIREBIRD II mission. *Journal of Geophysical Research: Space Physics*, 121(6):5272–5283. 2016JA022485.

Datta, S., Skoug, R., McCarthy, M., and Parks, G. (1997). Modeling of microburst electron precipitation using pitch angle diffusion theory. *Journal of Geophysical Research: Space Physics*, 102(A8):17325–17333.

Douma, E., Rodger, C., Blum, L., O'Brien, T., Clilverd, M., and Blake, J. (2019). Characteristics of relativistic microburst intensity from sampex observations. *Journal of Geophysical Research: Space Physics*.

Douma, E., Rodger, C. J., Blum, L. W., and Clilverd, M. A. (2017). Occurrence characteristics of relativistic electron microbursts from SAMPEX observations. *Journal of Geophysical Research: Space Physics*, 122(8):8096–8107. 2017JA024067.

Eastwood, J., Hietala, H., Toth, G., Phan, T., and Fujimoto, M. (2015). What controls the structure and dynamics of earths magnetosphere? *Space Science Reviews*, 188(1-4):251–286.

Greeley, A., Kanekal, S., Baker, D., Klecker, B., and Schiller, Q. (2019). Quantifying the contribution of microbursts to global electron loss in the radiation belts. *Journal of Geophysical Research: Space Physics*.

Hendry, A. T., Rodger, C. J., and Clilverd, M. A. (2017). Evidence of sub-mev emic-driven electron precipitation. *Geophysical Research Letters*, 44(3):1210–1218.

Horne, R., Glauert, S., Meredith, N., Boscher, D., Maget, V., Heynderickx, D., and Pitchford, D. (2013). Space weather impacts on satellites and forecasting the earth's electron radiation belts with spacecast. *Space Weather*, 11(4):169–186.

Horne, R. B., Thorne, R. M., Shprits, Y. Y., Meredith, N. P., Glauert, S. A., Smith, A. J., Kanekal, S. G., Baker, D. N., Engebretson, M. J., Posch, J. L., et al. (2005). Wave acceleration of electrons in the van allen radiation belts. *Nature*, 437(7056):227.

Kasahara, S., Miyoshi, Y., Yokota, S., Mitani, T., Kasahara, Y., Matsuda, S., Kumamoto, A., Matsuoka, A., Kazama, Y., Frey, H., et al. (2018). Pulsating aurora from electron scattering by chorus waves. *Nature*, 554(7692):337.

Klumpar, D., Springer, L., Mosleh, E., Mashburn, K., Berardinelli, S., Gunderson, A., Handly, M., Ryhajlo, N., Spence, H., Smith, S., Legere, J., Widholm, M., Longworth, S., Crew, A., Larsen, B., Blake, J., and Walmsley, N. (2015). Flight system technologies enabling the twin-cubesat firebird-ii scientific mission.

Lee, J. J., Parks, G. K., Lee, E., Tsurutani, B. T., Hwang, J., Cho, K. S., Kim, K.-H., Park, Y. D., Min, K. W., and McCarthy, M. P. (2012). Anisotropic pitch angle distribution of 100 keV microburst electrons in the loss cone: measurements from STSAT-1. *Annales Geophysicae*, 30(11):1567–1573.

Lee, J.-J., Parks, G. K., Min, K. W., Kim, H. J., Park, J., Hwang, J., McCarthy, M. P., Lee, E., Ryu, K. S., Lim, J. T., Sim, E. S., Lee, H. W., Kang, K. I., and Park, H. Y. (2005). Energy spectra of 170-360 keV electron microbursts measured by the korean STSAT-1. *Geophysical Research Letters*, 32(13). L13106.

Li, X., Selesnick, R., Schiller, Q., Zhang, K., Zhao, H., Baker, D. N., and Temerin, M. A. (2017). Measurement of electrons from albedo neutron decay and neutron density in near-earth space. *Nature*, 552(7685):382.

Lorentzen, K. R., Blake, J. B., Inan, U. S., and Bortnik, J. (2001a). Observations of relativistic electron microbursts in association with VLF chorus. *Journal of Geophysical Research: Space Physics*, 106(A4):6017–6027.

Lorentzen, K. R., Looper, M. D., and Blake, J. B. (2001b). Relativistic electron microbursts during the GEM storms. *Geophysical Research Letters*, 28(13):2573–2576.

Lyons, L. R. and Thorne, R. M. (1973). Equilibrium structure of radiation belt electrons. *Journal of Geophysical Research*, 78(13):2142–2149.

Meredith, N., Horne, R., Summers, D., Thorne, R., Iles, R., Heynderickx, D., and Anderson, R. (2002). Evidence for acceleration of outer zone electrons to relativistic energies by whistler mode chorus. In *Annales Geophysicae*, volume 20, pages 967–979.

Millan, R. and Thorne, R. (2007). Review of radiation belt relativistic electron losses. *Journal of Atmospheric and Solar-Terrestrial Physics*, 69(3):362 – 377.

Nakamura, R., Baker, D. N., Blake, J. B., Kanekal, S., Klecker, B., and Hovestadt, D. (1995). Relativistic electron precipitation enhancements near the outer edge of the radiation belt. *Geophysical Research Letters*, 22(9):1129–1132.

Nakamura, R., Isowa, M., Kamide, Y., Baker, D., Blake, J., and Looper, M. (2000). Observations of relativistic electron microbursts in association with VLF chorus. *J. Geophys. Res*, 105:15875–15885.

O'Brien, T., Claudepierre, S., Blake, J., Fennell, J. F., Clemmons, J., Roeder, J., Spence, H. E., Reeves, G., and Baker, D. (2014). An empirically observed pitch-angle diffusion eigenmode in the earth's electron belt near l*= 5.0. *Geophysical Research Letters*, 41(2):251–258.

O'Brien, T., Claudepierre, S., Guild, T., Fennell, J., Turner, D., Blake, J., Clemmons, J., and Roeder, J. (2016). Inner zone and slot electron radial diffusion revisited. *Geophysical Research Letters*, 43(14):7301–7310.

O'Brien, T. and Moldwin, M. (2003). Empirical plasmapause models from magnetic indices. *Geophysical Research Letters*, 30(4).

O'Brien, T. P., Looper, M. D., and Blake, J. B. (2004). Quantification of relativistic electron microburst losses during the GEM storms. *Geophysical Research Letters*, 31(4). L04802.

O'Brien, T. P., Lorentzen, K. R., Mann, I. R., Meredith, N. P., Blake, J. B., Fennell, J. F., Looper, M. D., Milling, D. K., and Anderson, R. R. (2003). Energization of relativistic electrons in the presence of ULF power and MeV microbursts: Evidence for dual ULF and VLF acceleration. *Journal of Geophysical Research: Space Physics*, 108(A8).

Ozaki, M., Miyoshi, Y., Shiokawa, K., Hosokawa, K., Oyama, S.-i., Kataoka, R., Ebihara, Y., Ogawa, Y., Kasahara, Y., Yagitani, S., et al. (2019). Visualization of rapid electron precipitation via chorus element wave–particle interactions. *Nature communications*, 10(1):257.

Parks, G. K. (1967). Spatial characteristics of auroral-zone X-ray microbursts. *Journal of Geophysical Research*, 72(1):215–226.

Reeves, G., Spence, H. E., Henderson, M., Morley, S., Friedel, R., Funsten, H., Baker, D., Kanekal, S., Blake, J., Fennell, J., et al. (2013). Electron acceleration in the heart of the van allen radiation belts. *Science*, 341(6149):991–994.

Reeves, G. D., McAdams, K. L., Friedel, R. H. W., and O'Brien, T. P. (2003). Acceleration and loss of relativistic electrons during geomagnetic storms. *Geophysical Research Letters*, 30(10):n/a–n/a. 1529.

Schulz, M. and Lanzerotti, L. J. (1974). *Particle Diffusion in the Radiation Belts*. Springer.

Seppälä, A., Douma, E., Rodger, C., Verronen, P., Clilverd, M. A., and Bortnik, J. (2018). Relativistic electron microburst events: Modeling the atmospheric impact. *Geophysical Research Letters*, 45(2):1141–1147.

Spence, H. E., Blake, J. B., Crew, A. B., Driscoll, S., Klumpar, D. M., Larsen, B. A., Legere, J., Longworth, S., Mosleh, E., O'Brien, T. P., Smith, S., Springer, L., and Widholm, M. (2012). Focusing on size and energy dependence of electron microbursts from the van allen radiation belts. *Space Weather*, 10(11).

Summers, D. (2005). Quasi-linear diffusion coefficients for field-aligned electromagnetic waves with applications to the magnetosphere. *Journal of Geophysical Research: Space Physics*, 110(A8):n/a–n/a. A08213.

Summers, D., Thorne, R. M., and Xiao, F. (1998). Relativistic theory of wave-particle resonant diffusion with application to electron acceleration in the magnetosphere. *Journal of Geophysical Research: Space Physics*, 103(A9):20487–20500.

Thorne, R. M., O'Brien, T. P., Shprits, Y. Y., Summers, D., and Horne, R. B. (2005). Timescale for MeV electron microburst loss during geomagnetic storms. *Journal of Geophysical Research: Space Physics*, 110(A9). A09202.

Trefall, H., Bjordal, J., Ullaland, S., and Stadsnes, J. (1966). On the extension of auroral-zone x-ray microbursts. *Journal of Atmospheric and Terrestrial Physics*, 28(2):225–233.

Tsurutani, B. T. and Lakhina, G. S. (1997). Some basic concepts of wave-particle interactions in collisionless plasmas. *Reviews of Geophysics*, 35(4):491–501.

Ukhorskiy, A. Y., Anderson, B. J., Brandt, P. C., and Tsyganenko, N. A. (2006). Storm time evolution of the outer radiation belt: Transport and losses. *Journal of Geophysical Research: Space Physics*, 111(A11):n/a–n/a. A11S03.

Van Allen, J. A. (1959). The geomagnetically trapped corpuscular radiation. *Journal of Geophysical Research*, 64(11):1683–1689.

Vernov, S. and Chudakov, A. (1960). Investigation of radiation in outer space. In *International Cosmic Ray Conference*, volume 3, page 19.

Walker, A. D. M. (1993). *Plasma waves in the magnetosphere*, volume 24. Springer Science & Business Media.